Contrib Mineral Petrol (2004) 146: 450–462
DOI 10.1007/s00410-003-0507-5

ORIGINAL PAPER

Kirill I. Shmulovich · Colin M. Graham

An experimental study of phase equilibria in the systems H_2O–CO_2–$CaCl_2$ and H_2O–CO_2–NaCl at high pressures and temperatures (500–800 °C, 0.5–0.9 GPa): geological and geophysical applications

Received: 12 September 2002 / Accepted: 8 July 2003 / Published online: 23 August 2003

Abstract Phase equilibria in the ternary systems H_2O–CO_2–NaCl and H_2O–CO_2–$CaCl_2$ have been determined from the study of synthetic fluid inclusions in quartz at 500 and 800 °C, 0.5 and 0.9 GPa. The crystallographic control on rates of quartz overgrowth on synthetic quartz crystals was exploited to prevent trapping of fluid inclusions prior to attainment of run conditions. Two types of fluid inclusion were found with different density or CO_2 homogenisation temperature ($T_h(CO_2)$): a CO_2-rich phase with low $T_h(CO_2)$, and a brine with relatively high $T_h(CO_2)$. The density of CO_2 was calibrated using inclusions in the binary system H_2O–CO_2. Mass balance calculations constrain tie lines and the miscibility gap between brines and CO_2-rich fluids in the H_2O–CO_2–NaCl and H_2O–CO_2–$CaCl_2$ systems at 500 and 800 °C, and 0.5 and 0.9 GPa. The miscibility gap in the $CaCl_2$ system is larger than in the NaCl system, and solubilities of CO_2 are smaller. $CaCl_2$ demonstrates a larger salting-out effect than NaCl at the same P–T conditions. In ternary systems, homogeneous fluids are H_2O-rich and of extremely low salinity, but at medium to high concentrations of salts and non-polar gases fluids are unlikely to be homogeneous. The two-phase state of crustal fluids should be common. For low fluid-rock ratios the cation compositions of crustal fluids are buffered by major crustal minerals: feldspars and micas in pelites and granitic rocks, calcite (dolomite) in carbonates, and pyroxenes and amphiboles in metabasites. Fluids in pelitic and granitic rocks are Na-K rich, while for carbonate and metabasic rocks fluids are Ca-Mg-Fe rich. On lithological boundaries between silicate and carbonate rocks, or between pelites and metabasites, diffusive cation exchange of the salt components of the fluid will cause the surfaces of immiscibility to intersect, leading to unmixing in the fluid phase. Dispersion of acoustic energy at critical conditions of the fluid may amplify seismic reflections that result from different fluid densities on lithological boundaries.

Editorial responsibility: I. Parsons

K. I. Shmulovich · C. M. Graham (✉)
School of Geo Sciences, University of Edinburgh,
West Mains Road, Edinburgh , EH9 3JW, UK
E-mail: colin.graham@glg.ed.ac.uk
Fax: 0131-668-3184

K. I. Shmulovich
Institute of Experimental Mineralogy,
Russian Academy of Sciences,
142432 Chernogolovka, Moscow, Russia

Introduction

Dissolved chloride salts are invariably present in hydrous fluids in the Earth's crust, sometimes in sufficiently large concentrations to produce hydrosaline melts (e.g. Shmulovich and Graham 1996; Aranovich and Newton 1996). While Na is the dominant cation in shallow saline groundwaters and formation waters, Ca is commonly the second most abundant cation and becomes the most abundant at high salinities, in deep wells drilled in sedimentary basins and crystalline rocks (White 1965; Kozlovsky 1984; Yardley and Graham 2002), and in mid-ocean ridge hydrothermal systems (e.g. Vanko et al. 1992). CO_2 is also a significant component of many deep crustal fluids, whose dissolution in H_2O-chloride fluids leads to unmixing of saline brines from CO_2-rich fluid (e.g. Shmulovich et al. 1995). In order to establish the geological extent and significance of the unmixing process, phase equilibria of fluids in the ternary systems H_2O–CO_2–NaCl and H_2O–CO_2–$CaCl_2$ must be determined and predictive thermodynamic models erected to span the wide range of crustal P–T–X(fluid) conditions.

Phase equilibria in the ternary system H_2O–CO_2–NaCl have been investigated at pressures up to 800 °C and 0.9 GPa (Kotel'nikov and Kotel'nikova 1990; Johnson 1991; Frantz et al. 1992; Joyce and Holloway 1993; Shmulovich et al. 1995; Shmulovich and Graham 1999), and PVT data for this system have been obtained by Gehrig (1980) and Gehrig et al. (1979) at pressures

below 0.06 GPa. Duan et al. (1995) constructed an equation of state for H_2O–CO_2–NaCl to ~1,000 °C, ~0.6 GPa and ~30 wt% NaCl, using experimental data of Gehrig (1980), Takenouchi and Kennedy (1965) and Frantz et al. (1992). Shmulovich and Graham (1999) used a modified synthetic fluid inclusion technique to determine phase equilibria in the ternary system at 800 °C and 0.9 GPa, constraining the region of immiscibility and the orientation of two-phase tie-lines. Their study provides important constraints on phase relations at high NaCl and CO_2 concentrations, showing that the solubility of CO_2 in brine is much smaller than predicted by the equation of state. The large compositional range of stability of halite + brine + CO_2-rich fluid in the ternary system is consistent with recent petrological and fluid inclusion studies of granulite facies rocks (e.g. Markl and Bucher 1998; Touret 1995).

Phase equilibria in the ternary system H_2O–CO_2–$CaCl_2$ have been determined at pressures and temperatures up to 0.5 GPa and 700 °C and at relatively low concentrations of CO_2 and $CaCl_2$ (Zhang and Frantz 1989; Shmulovich et al. 1995), revealing qualitatively similar phase relations and unmixing to those in the H_2O–CO_2–NaCl system. Shmulovich et al. (1995) found preliminary evidence at 500 °C for an initially decreasing and then increasing compositional field of unmixing with increasing pressure to 0.5 GPa.

In this paper, we present new experimental data for the ternary systems H_2O–CO_2–NaCl and H_2O–CO_2–$CaCl_2$ at 500 and 800 °C at 0.5 GPa, and for H_2O–CO_2–$CaCl_2$ at 800 °C and 0.9 GPa using a modified synthetic inclusion technique (Shmulovich and Graham 1999). Together with recently published data for the system H_2O–CO_2–NaCl at 800 °C, 0.9 GPa (Shmulovich and Graham 1999) and previously published data (reviewed in Shmulovich et al. 1995) these new data permit the identification of the P–T-X(fluid) region of immiscibility across practically all subsolidus crustal conditions and at high salinities and CO_2 concentrations. We use these results to obtain new insights into the geochemical and geophysical consequences of cation exchange and fluid unmixing in the deep crust.

Experimental techniques

High P–T experiments

Most experiments were conducted at the University of Edinburgh in internally heated gas pressure vessels (modified after Ford 1972) using an argon pressure medium. Pressure was measured using manganin pressure gauges calibrated periodically against the freezing point of mercury, the melting point of NaCl, and a Heise pressure gauge. Pressure measurements are considered to be accurate to ± 5 MPa. The duration of the 0.9 GPa runs was usually up to 5 days, during which time leakage of pressurised argon resulted in decrease of pressure from initial run pressures of 0.91–0.92 to ~0.88 GPa in some runs. Run pressures are taken as 0.9 ± 0.02 GPa. Run temperatures and temperature gradients were measured using two Pt/Pt13%Rh thermocouples positioned in the sample containers inside the furnaces so that the thermocouple tips were sited at one-third and two-thirds of the length of the capsules. Three capsules per run were placed around the thermocouples in a tantalum or molybdenum sample container. This arrangement gave a temperature gradient along the capsules of 5 °C (803 °C at the top of the capsule and 798 °C at the bottom), which was found to optimise mass transport and fluid inclusion formation. For a set thermocouple tip spacing, thermal gradients were modified by tilting of pressure vessels. The accuracy of temperature control was < ± 1 °C. Runs were heated at ~20°/min, and terminated by switching off the power, giving an initial quenching rate of ~100 °C/min, with ambient temperatures being reached in 800 °C runs within 4–5 min. Capsules remained pressurised in bombs for about 20 min after quenching to ensure temperature equilibration with cooling water (~10 °C) before depressurising and removal, and were then stored in ice to prevent leakage. The fugacities of hydrogen and oxygen in experiments were unbuffered, but the bomb walls and/or the ambient H_2 content of the argon pressure medium exert a buffering influence on water-bearing charges between Ni–NiO and Fe_2O_3–Fe_3O_4.

A few runs at 500 °C and 0.5 GPa were undertaken in externally heated nickel superalloy cold seal pressure vessels at the Institute of Experimental Mineralogy at Chernogolovka. Run durations for all runs in internally heated gas pressure vessels were 4–5 days at 800 °C and 2–3 weeks at 500 °C. Runs in cold-seal pressure vessels were of ~5 weeks' duration, because the capsules lie in low and unmeasured thermal gradients, resulting in slow mass transport. After quenching, capsules were checked for leaks and reweighed. Normal weight loss was ~0.3–0.5 mg depending on the mass of oxalic acid (see below), and resulted from hydrogen loss through Pt capsule walls.

Starting materials

Three main sources of CO_2 are available: liquid CO_2 (frozen into capsules at liquid N_2 temperatures), silver oxalate (AgC_2O_4) and oxalic acid dihydrate ($H_2C_2O_4.2H_2O$). For experiments in H_2O–CO_2-salt systems at low pressures using cold seal pressure vessels, the freezing method was used as a source of pure CO_2 (Shmulovich and Plyasunova 1993). This method requires relatively long capsules, which is not a problem for cold seal pressure vessels with a long (~40 mm) zone of low thermal gradient. However, the short capsules (20 mm) used for runs in internally heated gas pressure vessels exploded after filling with CO_2 at liquid nitrogen temperatures. Silver oxalate produces CO_2 and Ag only, but preliminary experiments showed that all fluid inclusions contained opaque daughter crystals, indicating that Ag is quite soluble in concentrated chloride solutions at high P and T (Zotov et al. 1995). Oxalic acid dihydrate produces equimolar quantities of H_2O and CO_2 together with 20 mol% of hydrogen at high P and T (Holloway et al. 1968). At 800 °C hydrogen diffuses readily through Pt capsules with wall thickness of 0.1 mm, and after 20 min at 800 °C the weight loss of the capsules corresponds to theoretical values. Therefore, oxalic acid dihydrate was used as the preferred source for CO_2 in this study.

The NaCl and SiO_2 gel were dried at 110 °C overnight before loading into Pt capsules. Oxalic acid dihydrate was stored in a desiccator. Pt capsules of 3-mm O.D. × 0.1-mm wall × ~20-mm length were loaded with quartz crystals, amorphous SiO_2 gel (12–15 mg), oxalic acid, NaCl powder and water, and welded by electric arc. Weight loss after welding was ≤ 0.1 mg. Weighing of $CaCl_2$ was a problem due to fast adsorption of water from air. The salt was removed from the container, placed into a funnel, pressed into the capsule, which was then placed in a glass container, sealed with a cork, and weighed. This procedure takes ~10–15 s. Weighing of $CaCl_2$ without a glass container shows that this time is sufficient to adsorb 0.05–0.1 mg H_2O (depending on air humidity). This value was added to the weight of $CaCl_2$, so that the correction was negligible. Water and oxalic acid were always loaded into capsules after $CaCl_2$.

Synthetic fluid inclusion technique

The synthetic fluid inclusion technique of Bodnar and Sterner (1987) was modified by Shmulovich and Graham (1999) in order to

decrease the trapping rate of fluid inclusions and thus to promote trapping of equilibrium fluids at run pressures and temperatures. A large, inclusion-free synthetic quartz crystal was used as a substrate for new quartz overgrowth hosting trapped fluid inclusions. The large crystal was sawn into small orientated crystals (~12–15×1.5×0.85 mm), with the Z-axis (the direction of maximum growth rate) orientated along the shortest dimension. The crystal surface with a width of 1.5 mm was scored by a diamond saw or by coarse SiC abrasive powder (100 mesh). Further abrasions were added using a large diamond crystal. After washing, each crystal was immersed in concentrated HF at 50–60 °C for about 30 min, re-washed and dried in a Pt crucible over a Bunsen flame.

After quenching, the quartz crystals were removed from the capsules and ground on one of the long faces (perpendicular to the X or Y axis) with microscopic control to protect the main plane of inclusions near the interface between overgrowth and substrate. Crystals were then polished on both sides and examined on the heating-freezing stage. Measurements of phase transformations in inclusions were made on a Linkam Scientific Instruments TMS-92 heating-freezing stage. For a general review of fluid inclusion techniques, see Roedder (1984).

Overheating sometimes resulted in non-reproducible homogenisation temperatures. Poor reproducibility of homogenisation temperatures of CO_2 [$T_h(CO_2)$] was observed for samples with $T_h(CO_2)$ below −25 °C. Because of the high density of CO_2, the pressure inside the inclusions increases along liquid CO_2 isochores and can attain 0.06–0.09 GPa. When walls of inclusions are thin (near the surface), they may be deformed by this pressure, and the inclusion volume may increase, resulting in a systematic increase in $T_h(CO_2)$. Normally, inclusions for examination were best preserved in abrasions in the surface of the substrate quartz on both sides of quartz crystals, and measurements could be made at one focal position of the lens.

The quartz crystals were overgrown by daughter quartz in a temperature gradient of ~5 °C along the capsule, and the interfaces contained numerous inclusions. These inclusions lie practically all in one plane (especially in 800 °C runs) making the measurement much easier. Slow growth of daughter quartz on these faces avoids the problem of pre-trapping of non-equilibrium fluid compositions during heating. The method of phase state measurement based on the varying density of liquid CO_2 in fluid inclusions (Sterner and Bodnar 1991) was described in detail for the ternary system H_2O–CO_2–NaCl at 800 °C and 0.9 GPa by Shmulovich and Graham (1999). When the fluid was quenched, $\rho(H_2O)$ evidently increased from 0.85 g cm^{-3} at 800 °C, 0.9 GPa to 1.0 g cm^{-3} at ambient conditions. The CO_2 density inside isolated fluid inclusions depends on the ratio H_2O/CO_2. When the fraction of water was high, the CO_2 density was low. The homogenisation of CO_2 could be measured much more easily and precisely than the clathrate melting temperature (see below; Shmulovich and Graham 1999) or the phase volume (solid:liquid:gas) ratio at room conditions.

Results

Phase equilibria at 800 °C, 0.5 GPa

Phase equilibria in the systems H_2O–CO_2–NaCl and H_2O–CO_2–$CaCl_2$ were studied by the same techniques as at 0.9 GPa (Shmulovich and Graham 1999). Fluid densities at 0.5 GPa are smaller than at 0.9 GPa, and fluid inclusions with high H_2O/CO_2 ratios have relatively low CO_2 density. Calibration experiments for CO_2 densities in the binary system H_2O–CO_2 at 800 °C, 0.5 GPa are presented in Fig. 1. On this diagram the actual range where fluid composition (CO_2 concentration) may be defined is limited to > 35 mass% of CO_2, since below this value the CO_2 concentration has too low

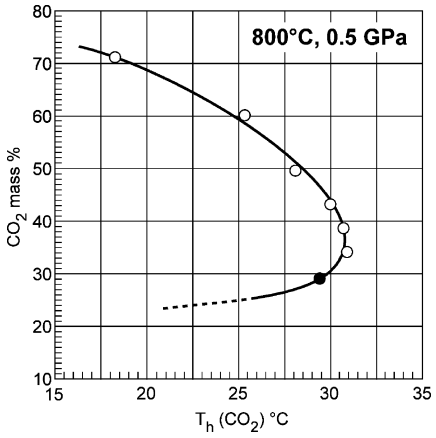

Fig. 1 Correlation between measured $T_h(CO_2)$ and concentration of CO_2 at 800 °C and 0.5 GPa in calibration runs in the binary system H_2O–CO_2. *Open circles* correspond to runs where CO_2 is homogenised to the liquid phase, *filled circles* to the gas phase. The critical point of CO_2 is at ~31 °C

a sensitivity to $T_h(CO_2)$ or homogenisation takes place into the gas phase (L + G⇒G). This process is observed as expansion of gas bubbles and slow disappearance of the liquid rim. Consequently, $T_h(CO_2)$ was usually measured only approximately. However, in some very flat inclusions or inclusions where liquid CO_2 condensed, these measurements could be made with acceptable precision. Only measurements of the phase transformation of L + G⇒L are included in Table 1.

The system H_2O–CO_2–NaCl

Table 1 displays experimental results in the system H_2O–CO_2–NaCl at 800 °C and 0.5 GPa. The phase compositions (CO_2-contents) were determined from measured $T_h(CO_2)$ values and the calibration diagram (Fig. 1). In some runs, two types of inclusions were found: a CO_2-rich phase with low $T_h(CO_2)$ and a brine with relatively high $T_h(CO_2)$. The problem of interpreting samples with a wide range of $T_h(CO_2)$ arises due to the possibility of trapping two phases in one inclusion in variable proportions. Where measurements are outliers from the main data set, the data are included in Table 1 but excluded from Fig. 2. Where the data are consistent, minimum values of $T_h(CO_2)$ were plotted as these data minimise the possibility of mixing of two different fluid phases. Measurement of $T_h(CO_2)$ together with mass balance permits estimation of the position of the phase boundary separating homogeneous one-phase fluid from the two-phase field.

The phase diagram for the system H_2O–CO_2–NaCl at 800 °C and 0.5 GPa is presented in Fig. 2. Runs 140 and 141 contain sufficient large inclusions within the quartz rim. The points on the phase boundary are determined from the intersection of two lines. One line passes through the bulk composition point and the point on the binary axis H_2O–CO_2 corresponding to the composition

Table 1 Bulk compositions, $T_h(CO_2)$ and CO_2 content of synthetic fluid inclusions after experiments at 800 °C, 0.5 GPa in the ternary system H_2O–CO_2–NaCl

Run no.	Fluid composition mass (%)			$T_h(CO_2)$ °C (L + G → L)			*n*	Phases of CO_2	Mass % CO_2
	CO_2	NaCl	H_2O	Min.	Mean	Max.			
110	44.7	37.0	37.0	15.5	16.5	18.9	7	LLGS → LLS	74
110				24.4	24.4	27.1	9	LLG → LL	60
111	37.0	35.9	27.1	27.8	28.2	28.4	11	LLG → LG(S)	50
111					16.4		1	LLGS → LLS	74
112	34.1	26.8	39.1					LGS	
113	53.5	24.6	21.9	21.2	22.6	22.6	3	LLGS → LLS	64
113				29.1	29.5	31.1	3	LLG → LL	45
114	50.1	18.6	31.3	18	20.1	20.9	7	LLGS → LLS	68
114				27.8	28.7	31.1	6	LLGS → LLS	49
115	40.9	14.9	44.2	30.5	30.7	30.9	17	LLG → LL	52
116	28.8	34.0	37.2	27	30.6	30.9	11	LLGS → LLS	38
117	41.25	15.75	43	26.4	27.1	28.4	18	LLG → LL	53
118	27.5	20.1	52.4					LGS	
119	71.0	0	29.0	18.2	18.5	18.7	19	LLG → LL	71
120	49.7	0	50.3	27.3	27.4	27.4	5	LLG → LL	52
121	29.0	0	71.0	25.5		25.6	7	LLG → LG	58
131	41.0	18.5	40.5						
132	30.6	25.9	43.5	26.9	27.0	27.6	9	LLG → LG	46
133	18.0	42.8	39.2	30.4	30.5	30.7	5	LLGS → LLS	41
137	43.2	0	56.8	30.0	30.2	30.3	7	LLG → LL	43
138	38.7	0	61.3	28.8	30.7	30.8	4		36
139	34.2	0	65.8			30.8	2	CRIT	33
140	37.3	23.1	39.6	29.7	29.8	29.9		LLG → LL	43
140				17	?	22.8	6	LLG → LL	74–64
141	38.5	27.9	33.6	20.4	20.7	23.4	3	LLG → LL	67
141				28.2	30.8	31.2	5	CRIT	33
142	59.9	0	40.1	25.2	25.3	26.5	14	LLG → LL	58

L Liquid, *S* solid, *G* gas, *n* number of measured inclusions

of the CO_2-rich phase as determined from Fig. 1 and $T_h(CO_2)$ for the CO_2-rich phase, fixing the orientation of the two-phase tie lines. The other line connects the point of CO_2 concentration in the NaCl-rich phase with the NaCl apex of the diagram. The intersection fixes the points on the phase boundary shown by the rectangles. As can be seen on Fig. 2, the slopes of tie lines for runs 111, 140 and 141 are very consistent. An independent check on the correctness of the phase diagram is the consistency of points on the phase boundary and the estimation of the NaCl saturation point of the brine composition.

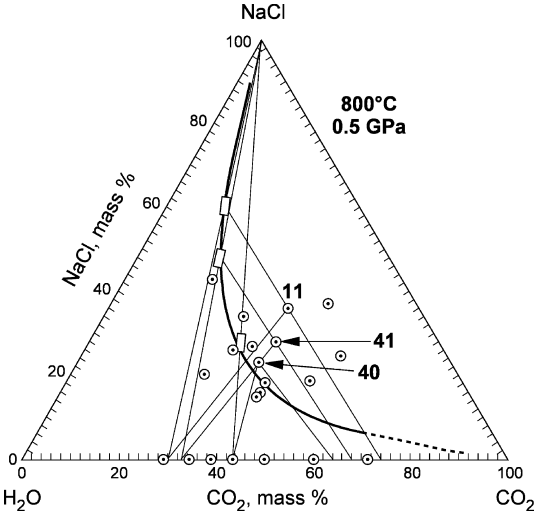

Fig. 2 Phase equilibria in the system H_2O–CO_2–NaCl at 800 °C and 0.5 GPa illustrating the results of experiments in Table 1. Data points (*open circles*) are bulk fluid compositions for each run. To simplify the diagram, *tie lines* are shown for only three bulk fluid compositions. The runs 111, 140 and 141 are marked as 11, 40 and 41 respectively. Size of *rectangles* for brine compositions for these runs corresponds to error interval. *Rectangles* are the points of intersection of lines connecting CO_2-rich compositions with bulk compositions, and salt-rich compositions with the NaCl apex

The system H_2O–CO_2–$CaCl_2$

Fluid inclusions in this system are more difficult to observe because at ambient temperatures there are three stable hydrates of $CaCl_2$ with two, four and six water molecules, and a relatively large volume of salt-rich inclusions is occupied by a solid phase. In addition, the similarity of the birefringence of quartz and some of these hydrates may obscure the boundary between the quartz host crystal and the inclusions. Finally, the application of the geometric method to estimate the position of phase boundaries must include a correction for CO_2 densities on the compression of water in the hydrate. The salt $CaCl_2$*$6H_2O$ is in equilibrium with saturated solution at $T < 30$ °C, and the molar volume of water in the salt is calculated from molar volume data (Lide 2002) to be 12.8 cm^3 mol^{-1}, only two-thirds of the liquid water volume.

Table 2 lists results of experiments in the ternary system H_2O–CO_2–$CaCl_2$ at 800 °C and 0.5 GPa,

Table 2 Bulk compositions, $T_h(CO_2)$, CO_2 contents and salinities (from clathrate melting) of synthetic fluid inclusions after experiments at 800 °C, 0.5 GPa in the ternary system H_2O–CO_2–$CaCl_2$

Run no.	Fluid composition mass (%)			$T_h(CO_2)$ °C		Mass % of CO_2		Mass % $CaCl_2$
	H_2O	CO_2	$CaCl_2$	→ L(n1)	→ G(n2)	CO_2–rich	Brine	
128	40.0	32.6	27.4	24.6(1)	29.4(1)	61	31	
129	33.1	39.9	27.0	22.3–24.9(14)	28.4(2)	64	30	8
134	33.9	22.4	43.7	23.2–26.4(9)	24–25(2)	66	28	
135	26.3	29.1	44.6	17.2–26(17)	27–30(2)	73	30	
136	22.4	34.2	43.4	21–23(4)	< 0	64	< 25	
143	26.4	34.0	39.6	18.4–21(16)	< 0	72	< 25	7
144	20.9	51.0	28.1	14.3–16.1(11)		76		
145	43.1	21.1	35.8	28.2–30.4(9)	28.2, 30.4(2)	51	30	15

L Liquid, *G* gas; *n1* and *n2* are numbers of measured inclusions; mass% $CaCl_2$ is estimation of salinity from clathrate melting temperatures

together with $T_h(CO_2)$ measurements and estimations of salinity of CO_2-rich fluid inclusions from the melting temperatures of clathrate (carbon dioxide hydrate: $CO_2.5.75H_2O$) which may form by reaction of CO_2 and H_2O in salt-poor fluids at low temperatures (Roedder 1984). All runs were made with bulk compositions in the two-phase field under run conditions. The geometrical treatment of the measurements follows that of Shmulovich and Graham (1999). The resulting phase diagram is shown in Fig. 3. Tie lines connect the bulk fluid compositions with points on the H_2O–CO_2 axis and extend towards the H_2O–$CaCl_2$ axis as far as their intersection with lines connecting the $CaCl_2$ apex with the CO_2 content of the salt rich phase. These intersection points define the miscibility gap to a good approximation. Diamonds indicate salinities of the CO_2-rich phase measured from clathrate melting temperatures. Corrections may be made for small salt concentrations in the CO_2-rich phase, i.e. tie lines intersect the boundary of the two-phase field with the equivalent CO_2 concentration rather than the H_2O–CO_2 axis. This correction will not significantly change the phase boundary but may modify slopes of tie lines. Correction for the extra volume for CO_2 expansion after cooling due to the low water volume in salt hydrate will shift the phase boundary toward the H_2O–$CaCl_2$ axis, but this shift is very difficult to estimate because we do not know the actual mixture of hydrate species. The same effect is predicted from the decreasing partial molar volume of water as a result of electrostriction on charged ions. The partial molar volume of water in the ternary system must be smaller than that in the binary H_2O–CO_2 system.

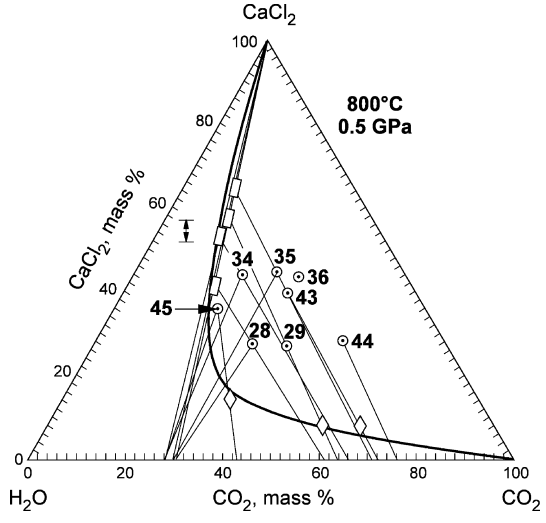

Fig. 3 Phase equilibria in the system H_2O–CO_2–$CaCl_2$ at 800 °C and 0.5 GPa, illustrating the results of experiments in Table 2. Last two digits of run numbers are shown. The *arrow* shows the range of salt concentrations from volume measurements in tube inclusions in run 134 (see text). The *thick line* is the phase boundary between one-phase and two-phase fluids (miscibility gap). *Tie lines* show the geometric approach to determining the phase boundary. *Diamonds* are salinities measured from clathrate melting temperatures; *open rectangles* are areas of uncertainty for points on the miscibility gap using the geometrical approach

An independent check on salt-rich compositions was possible for one run. Some runs were made using seed crystals and 2% solutions of Na_2CO_3 run for two days at 350 °C. After dissolution in this alkaline solution, long thin holes formed in the quartz crystals. Usually the inclusions in these holes were very difficult to observe. In the crystal from run 134 two closed tube inclusions were found with a length/width ratio of ~20. The CO_2 in these inclusions homogenised to a gas phase at 24–25 °C. At 30 °C the observed liquid:solid:gas phase ratios measured as volume ratios are very similar in both inclusions and equal to 55/25/20 (± 1). Saturated liquid in the system H_2O–$CaCl_2$ at 30 °C contains ~50 mass% salt (Lide 2002) and the equilibrium hydrate $CaCl_2$*$6H_2O$ contains 51.7 mass% (in fact, the composition of the hydrate could be $CaCl_2$*5.75 H_2O). If these inclusions contain equilibrium concentrations, the bulk salinity must be ~51 mass%. Unfortunately, metastable hydrates, especially $CaCl_2$*$4H_2O$ which has 60% $CaCl_2$, are prone to form in the system H_2O–$CaCl_2$ (Potter and Clynne 1978). Because mass exchange is very difficult in the thin tubes, parts of which were blocked by salt, we can expect that the solid phase is a mixture of the hexa- and tetra-hydrates, and the bulk salinity may be ~53 mass% $CaCl_2$. Calculation using an estimated density for saturated solution of ~1.4 g cm^{-3} gives a bulk concentration of 55 mass% if all of the solid phase is $CaCl_2$*$4H_2O$, showing that the bulk concentration is not very sensitive to the actual salt hydrate at the observed liquid/solid ratio. Intersection of the tie line for run 134 (Fig. 3) with the line connecting the CO_2 concentration in the brine takes place at a salinity of ~53 mass%. This value is

indistinguishable with that (52–55%) estimated from the volume ratios in the two long tube inclusions, confirming the correctness of the geometric approach in Fig. 3.

Attempts were made to measure the salinities of CO_2-rich inclusions from clathrate melting temperatures. Calibration of clathrate melting in the ternary system H_2O–CO_2–$CaCl_2$ (Shmulovich and Plyasunova 1993) indicates that the dependence of melting temperature on salinity in mass% is very similar to that in the system H_2O–CO_2–NaCl (Sloan 1990, see Figs. 4–22). Clathrate melting is practically invisible, and disappearance of the last clathrate was estimated from the convex curvature of the boundary between liquid CO_2 and salt solution. All measured temperatures lie between +1 and +6.5 °C, indicating that the salinity of CO_2-rich fluid in runs 129, 143 and 145 is in the range 7–15 mass% $CaCl_2$. The clathrate in 145 has a melting temperature of +1 °C (15% $CaCl_2$) and the CO_2 in the same inclusion homogenised to liquid at 30.2 °C, corresponding to a CO_2 content of 43 mass%. The maximum CO_2 concentration in the brine is 51 mass%, corresponding to a minimum $T_h(CO_2)$ of +28.2 °C. The measured salinities are shown by diamonds in Fig. 3 and the phase boundary was drawn to be consistent with all data.

Phase equilibria in the system H_2O–CO_2–NaCl at 500 °C, 0.5 GPa

Phase equilibria in the systems H_2O–CO_2–NaCl and H_2O–CO_2–$CaCl_2$ at 500 °C and O.5 GPa were measured by Shmulovich et al. (1995) using a simple heating-freezing stage with low quality optics. Clathrate melting temperatures were measured in two types of fluid inclusions, providing salinities but not CO_2 densities. The products of experiments in the H_2O–CO_2–$CaCl_2$ system (Shmulovich and Plyasunova 1993) were later re-examined in the CREGU laboratory (Nancy, France), providing sufficient experimental points to determine the miscibility gap, but in the H_2O–CO_2–NaCl system only four runs were in the two-phase field and the phase boundary was not reliably constrained. The main conclusion from comparison of the two ternary systems at 0.5 GPa and 500 °C was the similarity of the miscibility gaps (Shmulovich and Plyasunova 1993). However, more data are required to confirm this conclusion.

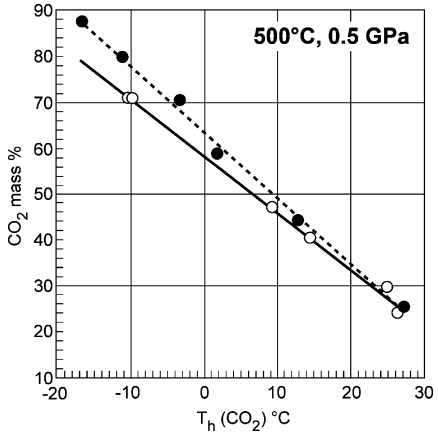

Fig. 4 Calibration curve for experiments in the binary H_2O–CO_2 system at 500 °C and 0.5 GPa. *Filled circles* after Sterner and Bodnar (1991); *open circles* this work. Our correlation is used for determination of CO_2 contents of inclusions in the ternary system

Some runs were undertaken to confirm the calibration curve of Sterner and Bodnar (1991) for H_2O–CO_2 at 500 °C and 0.5 GPa. A systematic deviation was observed between our calibration and that of Sterner and Bodnar (Fig. 4), perhaps as a result of using oxalic acid instead of silver oxalate as a source of CO_2. Possible reasons for this deviation are the admixture of hydrogen and nitrogen (from air) in our fluids, or the retention of some excess H_2 from oxalic acid decomposition in capsules at these temperatures. The melting temperature of CO_2 in our samples was usually between −58 and −62 °C, lower than the reference temperature (−56 °C). Because we also used oxalic acid for ternary system experiments, our calibration was used in preference to that of Sterner and Bodnar to estimate CO_2 concentration in ternary fluids. Use of silver oxalate as a source of CO_2 for ternary systems with halides results in large errors owing to the high solubility of AgCl. At 500 °C, quartz solubility in water and in brines is about one order of magnitude less than at 800 °C. Mass transport within run capsules is also smaller since the possibility of increasing the thermal gradient is limited at this temperature. Thus the thickness of quartz overgrowths and the quantity of fluid inclusions were much less than at 800 °C. To construct the phase diagram we used inclusions trapped in mechanical cracks near crystal boundaries. These cracks were expanded before runs by washing crystals in hot HF and drying at 350 °C.

Table 3 displays experimental results for runs at 500 °C, 0.5 GPa in the system H_2O–CO_2–NaCl. Runs 151 and 154 contain three types of inclusions (Fig. 5) due to incomplete equilibration of two salt solutions and the products of thermal dissociation of oxalic acid and/or the trapping in one inclusion of two different fluid compositions. Nonetheless, these data may be used to construct the phase diagram. Run 157 contains only one type of fluid inclusion, all of which homogenised over a narrow temperature interval. Consequently, the bulk composition lies in the one-phase field. Run 151 shows a Gaussian distribution of $T_h(CO_2)$ with a maximum close to 14 °C . Although experiment 154 has a similar distribution of $T_h(CO_2)$, the equilibrium state of the fluid is different.

The principal difference between these runs is the position of the inclusions. In run 154, seven inclusions with $T_h(CO_2)$ of −3 to −5 °C were found in the overgrowths; in run 151 all inclusions with $T_h(CO_2)$ around 10 °C and 20 °C belonged to a large population inside the crystal in which $T_h(CO_2)$ was usually ∼14 °C. CO_2-rich fluid was present at run conditions in 154 but this

Table 3 Bulk compositions, $T_h(CO_2)$ and CO_2 content of synthetic fluid inclusions after experiments at 500 °C, 0.5 GPa in the ternary system H_2O–CO_2–NaCl

Run no.	Fluid composition mass (%)			$T_h(CO_2)$ °C	*n*	Mass % of CO_2
	CO_2	NaCl	H_2O			L + G → L
147	62.3	9.2	28.5	24–25	8	28
148	54.6	11.1	34.3	25–26	7	27
149	47.1	12.9	40.0	2.5	2	55
149				19	16	34
151	27.5	17.7	54.8	6–19, (13.5)	29	34–51 (~42)
152	42.3	14.1	43.6	21–23	21	31–33
153	37.2	15.3	47.5	14–19	17	35–41
154	43.5	8.1	48.9	−5–+10	34	50–71
157	23.9	18.6	57.5	19–21	16	35
162	37.8	14.5	47.7	15.4–16.6	7	41
162				1–2.1	2	61
163	41.0	17.3	41.7	21.7	3	31
167	49.6	10.5	39.9	21–24	5	32
167				−2, +2	2	66

L Liquid, *G* gas, *n* number of measured inclusions

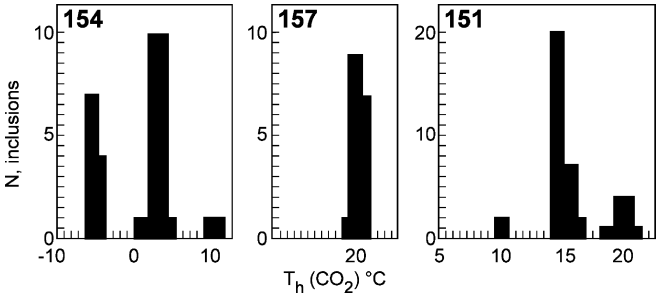

Fig. 5 Frequency distribution of $T_h(CO_2)$ for runs 151, 154 and 157. Run 157 is in the homogeneous one-phase field

was not the result of pre-trapping of unmixed fluids during heating to 500 °C. In run 149, two types of inclusion were found, but these were all inside the quartz crystal; therefore results of this run were ignored.

Figure 6 presents the geometrical basis for constraining the miscibility gap at 500 °C and 0.5 GPa. The phase diagram was initially constructed in the same manner as Figs. 2 and 3. After estimation of the NaCl content of the CO_2-rich phase, the slopes of tie lines were drawn with a correction to move the ends of the tie lines onto the phase boundary rather than the H_2O–CO_2 axis because salt saturation at 500 °C and 0.5 GPa occurs at 53 mass% NaCl and all experimental points lie close to the phase boundary. Without this correction the slopes of tie lines are too steep; thus, for example, the point for the NaCl rich phase for run 162 would lie above the saturation concentration.

Phase equilibria in the system H_2O–CO_2–$CaCl_2$ at 800 °C, 0.9 GPa

The system H_2O–CO_2–$CaCl_2$ was studied at 0.9 GPa and 800 °C by the same method as at 0.5 GPa.

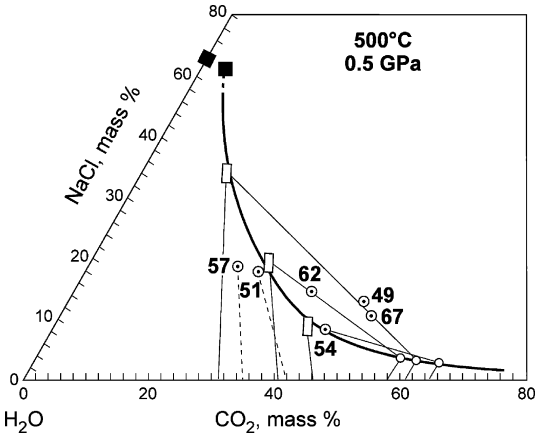

Fig. 6 Field of immiscibility in the system H_2O–CO_2–NaCl at 500 °C and 0.5 GPa, illustrating the results of experiments in Table 3. Last two digits of run numbers are shown. *Open circles* are bulk fluid compositions. *Rectangles* are points on the phase boundary based on the geometrical approach. *Small circles* are points corrected for salt concentration in CO_2 rich fluid. *Dashed lines* connect bulk compositions with average value of CO_2 (mass%) in the homogeneous fluid. *Filled square* indicates salt saturation under run conditions

Calibration of CO_2 densities in the binary H_2O–CO_2 at 0.9 GPa and 800 °C was from Shmulovich and Graham (1999). Bulk compositions and results of measurements of CO_2 homogenisation temperatures are presented in Table 4. Results for runs 91–93 and 95 were ignored as insufficient measurements were obtained; salt-rich inclusions were usually solid at room temperatures, and all inclusions where $T_h(CO_2)$ was estimated have a value of ~30–31 °C, i.e. near the critical point of CO_2. Run 94 is included in Table 4 and Fig. 7, but it is not clear what happens to fluid inside individual inclusions when $CaCl_2$ hydrates (S) and CO_2 (L + V) are in equilibrium at $T_h(CO_2)$. In a few inclusions we could measure $T_h(CO_2)$ corresponding to 60 mass% CO_2, and the dash-dot line connects the bulk fluid composition with this point on the diagram. The phase diagram of the system H_2O–CO_2–$CaCl_2$ at 0.9 GPa and 800 °C is shown in Fig. 7, where the run numbers (e.g. 1, 2) correspond to runs 101, 102 in Table 4. Runs 106–108 demonstrate a very narrow interval of $T_h(CO_2)$, and the bulk fluid compositions lie in the one-phase area. Runs 101–103 and 105 constrain three points on the miscibility gap using the geometrical approach, and because the boundary must pass between the bulk compositions of runs 105 and 106, the phase boundary may be drawn.

Phase diagrams for ternary systems at 0.5–0.9 GPa

Phase diagrams for the systems H_2O–CO_2–NaCl and H_2O–CO_2–$CaCl_2$ at pressures up to 0.3 GPa were studied by Zhang and Frantz (1989), Popp and Frantz (1979) and Kotel'nikov and Kotel'nikova (1990). Here we present diagrams for these systems at 0.5 and 0.9 GPa. Figures 2, 3, 6, 7 and equivalent diagrams for

Table 4 Bulk compositions, $T_h(CO_2)$ and CO_2 contents of synthetic fluid inclusions after experiments at 800 °C, 0.9 GPa in the ternary system H_2O–CO_2–$CaCl_2$

Run no.	Fluid composition mass (%)			$T_h(CO_2)$ °C				Mass % of CO_2	
	H_2O	CO_2	$CaCl_2$	*n*	Min.	*n*	Max.	CO_2-rich	Brine
94	13.9	34.0	52.1	3	−7(1)			60–62	
96	16.2	39.7	44.1	5	−25(1)	3	29.6	71–78	20
101	21.3	52.1	26.6	2	−15, −21	5	27.7–28.6	67–72	22
102	23.2	56.7	20.1	8	−20	3	27.6	72	22
103	24.7	39.8	35.5	2	−22.5	4	27(1)	73	23
104	30.8	37.1	32.1			11	25–27		23
105	36.9	33.2	29.9	4	−14	5	22–27	66	
106	46.2	30.9	22.9			4	9(0.3)	44	
107	49.1	29.2	21.7			6	11.4(0.5)	42	
108	50.6	25.3	24.1			7	15.7	37	

L Liquid, *G* gas; *n* numbers of measured inclusions; runs 91–95 (Table 1) all give $T_h(CO_2)$ of 30–31 °C, i.e. near critical point of CO_2; run 94 included in table and Fig 7, but measurements are anomalous; values in the brackets show deviation from given values if distribution is Gaussian

the system H_2O–CO_2–NaCl at 800 °C and 0.9 GPa (Shmulovich and Graham 1999) and for the system H_2O–CO_2–$CaCl_2$ at 500 °C and 0.5 GPa (Shmulovich and Plyasunova 1993) have been recalculated to mol% in Figs. 8, 9, 10. The saturation points in the binary systems were interpolated from reference data; a compilation of experimental data for the system H_2O–NaCl gives the saturation points as 73 mol% NaCl at 800 °C and 0.5 GPa, ~60 mol% at 800 °C and 0.9 GPa, and ~26 mol% at 500 °C and 0.5 GPa. In the system H_2O–$CaCl_2$ studied up to 180 °C equilibrium saturation occurs at 75 mass% of $CaCl_2$ with the peritectic reaction of dihydrate to monohydrate. The melting point of pure $CaCl_2$ is 772 °C. Consequently, the final dehydration reaction must occur between 180 and 772 °C. If the pressure dependence of the melting point of $CaCl_2$ is the same as in other salts (20–25 °C/0.1 GPa), T_m is ~880 °C at 0.5 GPa, and ~1,000 °C at 0.9 GPa. At low temperature, salt solubility is practically independent of pressure. From these arguments the saturation points for binary H_2O–$CaCl_2$ solutions were estimated as 90–95 mol% $CaCl_2$ at 800 °C and 0.5 GPa, 80–85 mol% at

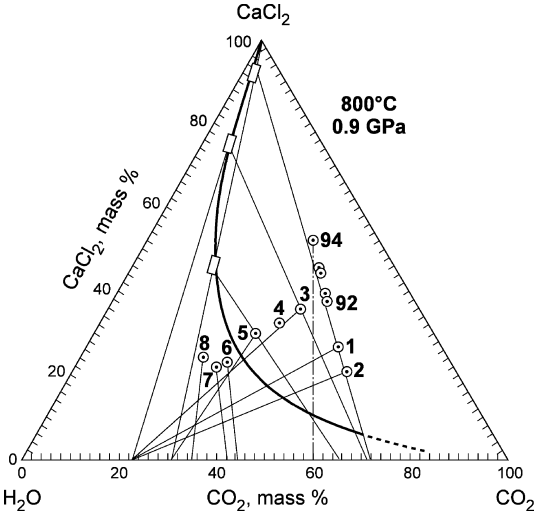

Fig. 7 Phase diagram for the system H_2O–CO_2–$CaCl_2$ at 0.9 GPa and 800 °C, illustrating the results of experiments in Table 4. The points marked as *1–8* correspond to runs 101–108 in Table 4. *Thin solid lines* indicate the geometrical approach. *Open circles* are bulk fluid compositions. *Dashed lines* connect bulk compositions with CO_2 concentrations for runs with one-phase fluid. *Dot-dash line* for run 94 shows the CO_2 concentration corresponding to $T_h(CO_2)$

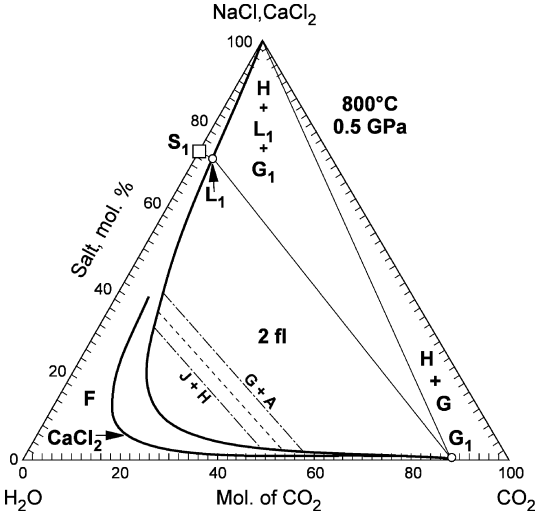

Fig. 8 Phase diagram for the systems H_2O–CO_2–NaCl and H_2O–CO_2–$CaCl_2$ at 800 °C and 0.5 GPa. *F* One-phase fluid; *2 fl* two-phase state; *H* is halite (or $CaCl_2$). *Square* (S_1) indicates halite saturation at 800 °C in the binary system H_2O–NaCl. Point L_1 indicates halite saturation in the ternary system; G_1 CO_2-rich phase, coexisting with L_1. *L* is phase with composition on line between S_1 and L_1; *G* between G_1 and CO_2 corner. *Dashed lines* show the slopes of tie lines from Fig. 2, *dot-dash lines* are tie lines after Joyce and Holloway (1993) for 700 °C, 0.5 GPa, and Geriy and Aranovich (personal communication) for 800 °C and 0.5 GPa

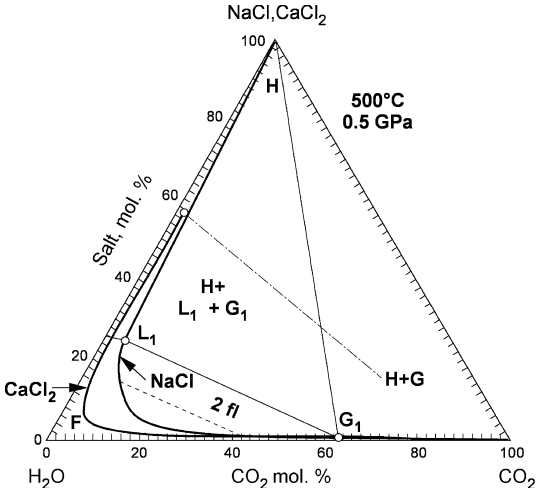

Fig. 9 Phase equilibria in the systems H_2O–CO_2–NaCl and H_2O–CO_2–$CaCl_2$ at 500 °C and 0.5 GPa. *Stability fields* are shown for H_2O–CO_2–NaCl system only. All legend as on Fig. 8

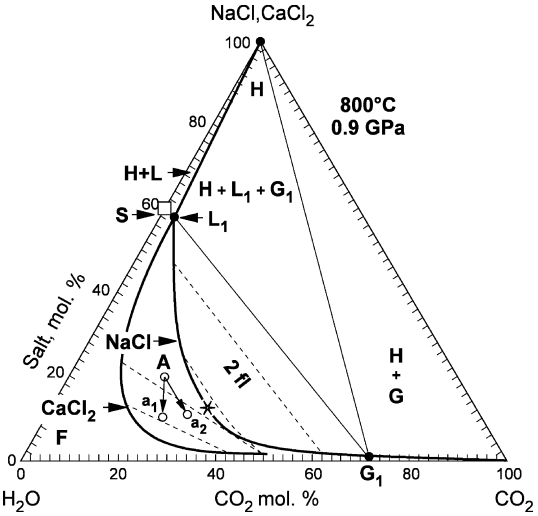

Fig. 10 Phase equilibria in the systems H_2O–CO_2–NaCl and H_2O–CO_2–$CaCl_2$ at 800 °C and 0.9 GPa. For the $CaCl_2$-bearing system only phase relations near to the critical point are shown. The critical point in the NaCl system is shown by (*). All legend as on Fig. 8. See text for discussion of points *A*, a_1 and a_2

800 °C and 0.9 GPa, and 50–55 mol% at 500 °C and 0.5 GPa.

The phase diagram for H_2O–CO_2–NaCl at 800 °C and 0.5 GPa is presented in Fig. 8. The diagram may be subdivided into five stability fields: one fluid (F); two coexisting fluids (2 fl); and three salt-saturated assemblages (H + L; H + L + G and H + G). This diagram is very similar to that at 800 °C and 0.9 GPa; however, the miscibility gap is larger. The slopes of tie lines were defined by the compositions of coexisting fluid inclusions and are very consistent with independent measurements (Joyce and Holloway 1993) and calculations based on water activities in brine and H_2O–CO_2 mixtures (Geriy and Aranovich, personal communication).

Phase equilibria at 500 °C and 0.5 GPa are shown in Fig. 9. The principal differences between the systems at 500 °C compared to 800 °C are: (1) a shift in the miscibility gap towards the H_2O apex; (2) a major reduction of two-phase (L + G) field at 500 °C; (3) a strong reduction of the fields with undersaturated solution as a result of limited salt solubilities at 500 °C; and (4) smaller slopes of tie lines relative to the H_2O–CO_2 axis at 500 °C.

For the same phase diagram topology, the boundaries of phase assemblages depend mainly on the temperature coefficients of salt solubility and saturation points. We can expect that at 500 °C the salt dissociation rate is larger than at 800 °C, and the concentrations of ions will also be larger. Consequently, water activity will be smaller at 500 °C. In this case, the slopes of tie lines relative to the H_2O–CO_2 axis will also be smaller, since for the same H_2O/CO_2 in the coexisting gas phase the brine contains more H_2O. The same effect is predicted from comparison of the influence of different salts on water activity: electrostriction of water on ions will be stronger with Ca^{2+} than Na^+, water activity in H_2O–$CaCl_2$ will be smaller than in H_2O–NaCl, and the slopes of tie-lines relative to the H_2O–CO_2 axis will be smaller in the H_2O–$CaCl_2$ system. This effect is well illustrated in Fig. 10 where the system H_2O–CO_2–$CaCl_2$, recalculated from Fig. 7, is compared with the H_2O–CO_2–NaCl system at 800 °C and 0.9 GPa (Shmulovich and Graham 1999). The greater compositional range of two-phase (L + G) fluids in H_2O–CO_2–$CaCl_2$ compared to H_2O–CO_2–NaCl is evident in each P–T section (Figs. 8, 9, 10).

The effect of pressure on phase equilibria at 800 °C from 0.5 to 0.9 GPa is not large. The salt concentration of saturated solutions increases as the melting points of pure salts increase (at 20–25 °C/0.1 GPa). Consequently, the point L_1 is shifted towards the H_2O apex at higher pressure. The miscibility gaps are larger as a result of the shift of points L_1 and G_1; this effect is partly compensated by the shift of the near-critical area out from the H_2O apex.

One interesting phenomenon is observed from a comparison of Figs. 8 and 10. At a salinity of $\geq\sim$30 mol%, CO_2 solubility in brines is larger at 0.5 GPa than at 0.9 GPa. This may be an artefact of systematic overestimation of CO_2 solubility in concentrated brines at 0.5 GPa, where: (1) homogenisation of CO_2 takes place into the gas phase and is usually difficult to observe; (2) at high fluid salinity, CO_2 is more dense (more CO_2 per unit volume) at run conditions, due to water compression around salt ion pairs, than is expected for the same H_2O/CO_2 ratio in the binary system. Thus CO_2 concentrations from Fig. 1 estimated for the ternary systems may be overestimated. If this small effect is real, then the salting-out effect increases with increasing pressure from 0.5 to 0.9 GPa at 800 °C when water density increases from 0.7 to 0.88 g cm^{-3}. Xie and Walther (1993) show from quartz solubility in salt solutions that below 0.2 GPa the salting-out effect changes to a salting-in effect with increasing temperature. Thus at constant pressure, decreasing fluid density is accompanied by a decreasing salting-out effect and

vice versa. Exactly the same relations are observed here: isothermal increase in density from 0.5 to 0.9 GPa is accompanied by an increasing salting-out effect.

Fluid unmixing and critical phenomena near lithological boundaries

Figures 8, 9 and 10 illustrate the very limited range of homogeneous, single-phase H_2O–CO_2-brine fluids which are stable under typical conditions of deep crustal metamorphism (500–800 °C, 0.5–0.9 GPa). These fluids are largely restricted to H_2O-rich compositions. Fluid unmixing into a two-phase state (brine + CO_2-rich fluid) may occur by changing P and T, and by changing fluid composition through modifying the proportions of H_2O, CO_2 and brine (NaCl, $CaCl_2$). In addition, the more extensive field of unmixing of H_2O–CO_2–$CaCl_2$ fluids relative to H_2O–CO_2–NaCl fluids at any P–T also indicates that change in cation composition of ternary H_2O–CO_2–brine fluids, for example by cation exchange, may lead to a change in phase state from single-phase to two-phase fluid. We now examine in more detail how changes in fluid phase state may occur during fluid-rock interaction at lithological boundaries, and the geophysical consequences of these processes.

Consider a lithological boundary between carbonate or basic rock and a quartzo-feldspathic or pelitic rock in the presence of a ternary H_2O–CO_2-brine fluid under metamorphic conditions, a common geological situation. In a rock-dominated fluid-rock system, the cation composition of the fluid depends on the composition and mineralogy of the host rocks. For a constant Cl concentration, the fluid in the quartzo-feldspathic rock will have dominantly Na-K cations, and the carbonate or basic rock dominantly Ca ($\pm$Mg, Fe) cations. Interconnectivity of this pore fluid at and across the lithological boundary by either diffusive or advective transport, whether via grain-edge flow (e.g. Watson and Brenan 1987; Holness 1997) or hydrofracture (e.g. Walther and Orville 1982), will lead to cation exchange if solid-fluid equilibration is rapid. Advective fluid transport will be relatively rapid and result in a geochemical front, broadened by dispersion, with typical fluxes estimated for cross-layer flow of 10^{-10} to 10^{-13} m s^{-1} (Skelton et al. 1997). Diffusion through a static, interconnected pore fluid will be relatively slow, since the diffusion coefficient in aqueous solutions is around 10^{-4}–10^{-5} m^2 s^{-1} (Balashov 1995). Thus the field of fluid unmixing should be stable and close to lithological boundaries. Irrespective of the mechanism, the change in cation composition of the fluid along the diffusion profile or advection pathway should result in the occurrence of unmixing in the fluid near a lithological boundary of this type. An aqueous two-phase H_2O–CO_2–$CaCl_2$ fluid (A) in a carbonate-rich or basic rock contains brine (L) + CO_2-rich fluid (G), while at the same P and T the H_2O–CO_2–NaCl fluid of comparable Cl concentration in an adjacent quartzo-feldspathic rock is homogeneous (Fig. 10). Along an interconnected fluid pathway between the two lithologies, the homogeneous fluid phase will become heterogeneous, and gas bubbles will appear. Depending on whether Na is incorporated into solid (feldspar) or fluid during exchange, the exchange reaction can be represented as:

1. $2NaCl(aq) + CaAl_2Si_2O_8 + 4SiO_2 = CaCl_2(aq) + 2NaAlSi_3O_8$

or

2. $2NaCl(aq) + CaCO_3 + H_2O = CaCl_2(aq) + 2NaOH + CO_2$

In reaction (1) the fluid bulk composition is shifted from composition "A" (20 mol% NaCl, 20 mol% CO_2, 60 mol% H_2O) in a direction away from the NaCl apex to point "a_1" (see Fig. 10) and in reaction (2) towards the CO_2 apex, to point "a_2". Irrespective of whether the starting fluid is homogeneous or on the two-phase surface, every fluid phase evolves by the same process.

The change of phase state during cation exchange between fluid and buffering host rocks takes place over a wide interval of P, T and X(fluid) conditions, but the compositional limits for this phenomenon depend on P and T. For example from Fig. 10, the limiting conditions for unmixing events on boundaries between Na-rich and Ca-rich lithologies at 800 °C and 0.9 GPa may be estimated as $0.4 < X(H_2O) < 0.7$ and X(NaCl eq.) > 0.04. At 500 °C and 0.5 GPa the equivalent limits are $\sim 0.5 < X(H_2O) < 0.9$ and X(NaCl eq.) > 0.2. These compositions are geologically realistic, although there are few data on the composition and quantity of fluid in the lower crust. Different models lead to different conclusions. Stevens and Clemens (1993) and Yardley and Valley (1997) consider the lower crust to be practically 'dry' following formation of the characteristic metamorphic mineral assemblages. Aranovich and Newton (1997), Frost and Wood (1997) and Shmulovich and Graham (1996) consider that the formation of hydrous minerals (e.g. biotite and amphiboles) in subsolidus assemblages requires the presence of a fluid or melt phase. Depressed advection and much higher diffusion rate (compared to infiltration rate) are both conditions favourable for the occurrence of unmixing near lithological boundaries, particularly in low permeability rocks of the lower crust.

The new results of this study enable us to consider the evolution of a metamorphic fluid with increasing temperature from initial dehydration of clay at very low grade (Yardley 1996). Prograde heating and dehydration generates a fluid with high $X(H_2O)$. The salinity of a metamorphic fluid may be increased by hydration and melting reactions, by fluid unmixing, and by dissolution of evaporitic minerals, and decreased by dehydration, water infiltration and melt crystallisation. Fluids of even modest salinity at high P and T will unmix into a dense CO_2-rich phase and brine. The former are typical of fluid

inclusions in granulite facies rocks (e.g. Coolen 1982; Touret 1985; Herms and Schenk 1998). Evidence of the latter has been reported in the same granulite facies rocks in Norway (Touret 1995). Recently solid (Na,K)Cl inclusions have been found in granulite and eclogite facies rocks in Norway, probably indicating the final stages of fluid desiccation (Markl and Bucher 1998). All these inclusions correspond to the sections of the ternary diagrams in Figs. 8, 9, 10, that lie to the right of the L_1-G_1 tie line. If a metamorphic fluid evolves from an initially hydrous fluid to a mixture of CO_2-rich fluid + dry salts ± brine, then the formation and exsolution of fluid near lithological boundaries will occur during this evolution.

Similar unmixing phenomena will occur at lithological boundaries between metabasic and quartzo-feldspathic (or pelitic) rocks to those at carbonate-pelite boundaries. In metabasites, cation composition will be determined by mineral-fluid equilibria involving pyroxene and amphiboles, and will include Mg and Fe in addition to Ca. Although the phase equilibria will be modified relative to Fig. 3, the possibility of fluid unmixing still exists.

The geophysical consequences of fluid unmixing at lithological boundaries

Extensive seismic reflection profiling has revealed numerous prominent sub-horizontal seismic reflectors in the middle and lower continental crust. Perhaps the most striking deep crustal reflector was identified by the Consortium for Continental Reflection Profiling (COCORP) reflection survey in the Wind River Mountains, USA (Oliver 1990). The lithological and physical properties responsible for strong seismic reflection (reflection coefficients $R \geq \sim 0.1$) remain uncertain. The two main hypotheses are related to the presence of deep crustal faults; these are high pore-fluid pressure and texture-induced anisotropy of deformed rocks (e.g. Jones and Nur 1984). Results of seismic modelling (Shapiro and Hubral 1996) have indicated that variations in layer thickness of laminar structures can also produce relatively strong reflections by constructive interference. However, extensive studies of texture-induced anisotropy in mylonites including laboratory acoustic experiments under in-situ conditions have not provided a conclusive answer. Theoretical simulations suggest that strong seismic reflections with reflection coefficient $R \approx 0.1$ are generally not a result of preferred orientations of anisotropic minerals or open cracks supported by high pore-fluid pressure alone, but must be significantly enhanced by changes in lithology. Similarly, special variations in layer thickness of laminar structures are needed to explain strong seismic reflections by constructive interference.

On the other hand the combination of lithology with high pore-fluid pressure can give rise to reflection coefficients of the order of $R \approx 0.1$ even for pore-fluid with the physical properties of water under lower crust P–T conditions. It has been shown (Zatsepin and Crampin 1997) that velocities of seismic P- and S-waves depend drastically on the pore-fluid compressibility when pore-fluid pressure is close to the minimum value of principal differential stress in rocks. The critical behaviour of fluid is generally accompanied by abnormal (very high) values of fluid compressibility. This behaviour may be easily defined in simple one-component systems. For a more realistic three-component model metamorphic fluids (Figs. 8, 9, 10) critical points at constant P and T are the points where tie lines shrink to one point; these compositions will only be coincidentally realised in nature. A much more likely scenario is that abnormal compressibility is the result of a metastable state.

We have argued that fluid present across a lithological boundary might contain a diffusion profile resulting from cation exchange (Na,K) < – > (Ca,Mg,Fe). Somewhere between the two (L + G) miscibility gaps in Figs. 8, 9 and 10, the concentration ratio of monovalent to divalent cations will correspond to equilibrium. At equilibrium, a second fluid phase may appear with a composition at the opposite end of the equilibrium tie line. However, supersaturation is required for nucleation of this second fluid. The rate of supersaturation depends on various parameters, notably on the interface surface tension. The diffusion process is continuous up to an equilibrium concentration of each cation, whereas the limit of supersaturation depends on the internal properties of the fluid. The second fluid phase will nucleate periodically and separate under gravity, and this process will occur repeatedly. Acoustic energy can initiate nucleation of the second fluid phase and be adsorbed in the process. The nucleation and separation will continue for as long as interconnected fluid is present and cation diffusion continues. This mechanism will result in a very high impedance contrast at a lithological boundary when the fluid is in a critical state. The mechanism cannot be responsible for seismic reflections attributed to mylonitic fault zones, but can provide an independent explanation for numerous deep crustal reflections in various geological provinces.

Critical unmixing phenomena at lithological boundaries lead to dispersion of acoustic energy and thus to amplification of seismic reflection even when rock layers have similar densities. At the front of compression waves the "gas" bubbles will collapse as the homogeneous area in Fig. 10 (F) increases with pressure. In the rarefied wave that follows, the bubbles will appear again but a certain degree of supersaturation is needed for nucleation. These critical phenomena delay the dissipation of acoustic energy and create the reflection of seismic waves without large difference in rock densities. In principle, similar effects could be achieved in homogeneous rocks if fluid unmixing takes place after crossing the phase boundary along the P–T trend of the ambient geothermal gradient or as a result of fluid evolution following chemical reactions and/or

melting. Further (acoustic) experiments are required to predict the role of these phenomena in seismic reflection in the lower crust.

Acknowledgements We thank Bruce Yardley for regular discussions and the use of heating–freezing stage facilities at the University of Leeds; Steve Elphick and Bob Brown for laboratory and workshop support and advice; Sergei Zatsepin for discussion of the interpretation of mechanisms of seismic reflection. Helpful reviews by John Holloway and Ian Parsons are gratefully acknowledged. This study was supported by NERC Research Grant GR3/12910.

References

Aranovich LYa, Newton RC (1996) H_2O activity in concentrated NaCl solutions at high pressures and temperatures measured by the brucite-periclase equilibrium. Contrib Mineral Petrol 125:200–212

Aranovich LYa, Newton RC (1997) H_2O activity in concentrated KCl and KCl–NaCl solutions at high temperatures and pressures measured by the brucite-periclase equilibrium. Contrib Mineral Petrol 127:261–271

Balashov VN (1995) Diffusion of electrolytes in hydrothermal systems: free solution and porous media. In: Shmulovich KI, Yardley BWD, Gonchar G (eds) Fluids in the crust. Chapman and Hall, London, pp 215–251

Bodnar RJ, Sterner SM (1987) Synthetic fluid inclusions. In: Ulmer G, Barnes HL (eds) Hydrothermal experimental techniques. Wiley, New York, pp 423–457

Coolen JJMMM (1982) Carbonic fluid inclusions in granulites from Tanzania—a comparison of geobarometric methods based on fluid density and mineral chemistry. Chem Geol 37:59–77

Duan Z, Moller N, Wear JH (1995) Equation of state for NaCl–H_2O–CO_2 system: prediction of phase equilibria and volumetric properties. Geochim Cosmochim Acta 59:2869–2882

Ford CE (1972) Furnace design, temperature distribution, calibration and seal design in internally heated pressure vessels. Progr Exp Petrol, Natural Environment Research Council (UK) Publ D2, pp 89–96

Frantz JD, Popp RK, Hoering TC (1992) The compositional limits of fluid immiscibility in the system H_2O–NaCl–CO_2 as determined with the use of synthetic fluid inclusions in conjunction with mass spectrometry. Chem Geol 98:237–255

Frost DJ, Wood BJ (1997) Experimental measurements of the properties of H_2O–CO_2 mixtures at high pressures and temperatures. Geochim Cosmochim Acta 61:3301–3309

Gehrig M (1980) Phasengleichgewichte und PVT-Daten ternarer Misschungen aus Wasser, Kohlendioxid und Natriumchlorid bis 3 kbar und 550 °C. Doctoral Diss, Karlsruhe University

Gehrig M, Lentz H, Franck EU (1979) Thermodynamic properties of water-carbon dioxide-sodium chloride mixtures at high temperatures and pressures. In: Timmerhaus KD, Barber MS (eds) High-pressure science and technology. Plenum, New York, pp 534–542

Herms P, Schenk V (1998) Fluid inclusions in high-pressure granulites of the Pan-African belt in Tanzania (Uluguru Mts): a record of prograde to retrograde fluid evolution. Contrib Mineral Petrol 130:199–212

Holloway JR, Burnham CW, Millhollen GL (1968) Generation of H_2O–CO_2 mixtures for use in hydrothermal experimentation. J Geophys Res 73:6598–6600

Holness MB (1997) Surface chemical controls on pore-fluid connectivity in texturally equilibrated materials. In: Jamtveit B, Yardley BWD (eds) Fluid flow and transport in rocks. Chapman and Hall, London, pp 149–169

Johnson EL (1991) Experimentally determined limits for H_2O–CO_2–NaCl immiscibility in granulites. Geology 19:925–928

Jones T, Nur A (1984) The nature of seismic reflections from deep crustal fault zones. J Geophys Res 89:3153–3171

Joyce DB, Holloway JR (1993) An experimental determination of the thermodynamic properties of H_2O–CO_2–NaCl fluids at high pressures and temperatures. Geochim Cosmochim Acta 57:733–746

Kotel'nikov AR, Kotel'nikova ZA (1990) An experimental study of the phase state of the system H_2O–CO_2–NaCl using synthetic fluid inclusions in quartz. Geokhimia 4:526–537

Kozlovsky EA (1984) Study of the deep structure of continental crust by drilling of the Kola superdeep borehole (in Russian). Nedra, Moscow, 490 pp

Lide D (ed) (2002) CRC Handbook of chemistry and physics, 82nd edn. CRS Press, Boca Raton

Markl G, Bucher K (1998) Composition of fluids in the lower crust inferred from metamorphic salt in lower crust. Nature 391:781–783

Oliver JE (1990) COCORP and fluids in the crust. In: Bredehoeft JD, Norton D (eds) The role of fluids in crustal processes. Natl Acad Press, Washington, DC, pp 128–139

Popp RK, Frantz JD (1979) Mineral-solution equilibria, II. An experimental study of mineral solubilities and the thermodynamic properties of aqueous $CaCl_2$, in the system CaO–SiO_2–H_2O–HCl. Geochim Cosmochim Acta 43:1777–1790

Potter RW, Clynne MC (1978) Solubility of highly soluble salts in aqueous media, Part I. NaCl, KCl, $CaCl_2$, Na_2SO_4, and K_2SO_4 solubilities to 100 °C. J Res US Geol Surv 6:701–703

Roedder E (1984) Fluid inclusions. Miner Soc Am, Rev Mineral 12

Shapiro SA, Hubral P (1996) Elastic waves in finely layered sediments: the equivalent medium and generalized O'Doherty-Anstey formulas. Geophysics 61:1282–1300

Shmulovich KI, Graham CM (1996) Melting of albite and dehydration of brucite in H_2O–NaCl fluids to 9 kbars and 700–900 °C: implications for partial melting and water activities during high pressure metamorphism. Contrib Mineral Petrol 124:370–382

Shmulovich KI, Graham CM (1999) An experimental study of phase equilibria in the system H_2O–CO_2–NaCl at 800 °C and 9 kbar. Contrib Mineral Petrol 136:2457–257

Shmulovich KI, Plyasunova NV (1993) High-temperature high-pressure phase equilibria in the ternary system H_2O–CO_2–salt ($CaCl_2$, NaCl). Geokhimia 5:666–684

Shmulovich KI, Tkachenko SI, Plyasunova NV (1995) Phase equilibria in fluid systems at high pressures and temperatures. In: Shmulovich KI, Yardley BWD, Gonchar G (eds) Fluids in the crust. Chapman and Hall, London, pp 193–214

Skelton ADL, Bickle MJ, Graham CM (1997) Fluid-flux and reaction rate from advective-diffusive carbonation of mafic sill margins in the Dalradian, southwest Scottish Highlands. Earth Planet Sci Lett 146:527–539

Sloan ED (1990) Natural-gas-hydrate phase equilibria and kinetics—understanding the state-of-the-art. Rev I Fr Petrol 45:245–266

Stevens G, Clemens JC (1993) Fluid-absent melting and the roles of fluids in the lithosphere: a slanted summary? Chem Geol 108:1–17

Sterner SM, Bodnar RJ (1991) Synthetic fluid inclusions. X. Experimental determination of P-V-T-X properties in the CO_2–H_2O system to 6 kbar and 700 °C. Am J Sci 291:1–54

Takenouchi S, Kennedy GC (1965) The solubility of carbon dioxide in NaCl solutions at high temperatures and pressures. Am J Sci 263:445–454

Touret J (1985) Fluid regime in southern Norway: a record of fluid inclusions. In: Tobi AC, Touret JLR (eds) The deep Proterozoic crust in the north Atlantic provinces. NATO ASI Series C158, Reidel, Dordrecht, pp 517–549

Touret JLR (1995) Brines in granulites: the other fluid. Bol Soc Esp Mineral 18(1):250–251

Vanko DA, Griffith JD, Erickson CL (1992) Calcium-rich brines and other hydrothermal fluids in fluid inclusions from plutonic rocks, Oceanographer Transform, Mid-Atlantic Ridge. Geochim Cosmochim Acta 56:35–47

Walther JV, Orville PM (1982) Volatile production and transport in regional metamorphism. Contrib Mineral Petrol 79:252–257

Watson EB, Brenan JM (1987) Fluids in the lithosphere, I. Experimentally-determined wetting characteristics of CO_2–H_2O fluids and their implications for fluid transport, host-rock physical properties, and fluid inclusion formation. Earth Planet Sci Lett 85:497–515

White DE (1965) Saline waters in sedimentary rocks. Am Assoc Petrol Geol Mem 4:342–366

Xie Z, Walther JV (1993) Quartz solubilities in NaCl solutions with and without wollastonite at elevated temperatures and pressures. Geochim Cosmochim Acta 57:1947–1955

Yardley BWD (1996) The evolution of fluids through the metamorphic cycle. In: Jamtveit B, Yardley, BWD (eds) Fluid flow and transport in permeable rocks. Chapman and Hall, London, pp 99–119

Yardley BWD, Graham JT (2002) The origins of salinity in metamorphic fluids. Geofluids, in 2:249–256

Yardley BWD, Valley JW (1997) The petrological case for a dry lower crust. J Geophys Res 102:12173–12185

Zatsepin SV, Crampin S (1997) Modelling the compliance of crustal rocks: I – response of shear-wave splitting to differential stress. Geophys J Int 129:477–494

Zhang Y-G, Frantz JD (1989) Experimental determination of the compositional limits of immiscibility in the system $CaCl_2$–H_2O–CO_2 at high temperatures and pressures using synthetic fluid inclusions. Chem Geol 74:289–308

Zotov AV, Kudrin AV, Levin KA, Shikina ND, Var'yash LN (1995) Experimental studies of the solubility and complexing of selected ore elements (Au, Ag, Cu, Mo,As, Sb, Hg) in aqueous solutions. In: Shmulovich KI, Yardley BWD, Gonchar G (eds) Fluids in the crust. Chapman and Hall, London, pp 95–138